Ligand structure and mechanical properties of single-nanoparticle-thick membranes

K. Michael Salerno, Dan S. Bolintineanu, J. Matthew D. Lane, and Gary S. Grest

Phys. Rev. E **91**, 062403 — Published 16 June 2015

DOI: 10.1103/PhysRevE.91.062403

Ligand structure and mechanical properties of single-nanoparticle thick membranes

K. Michael Salerno,[1] Dan S. Bolintineanu,[1] J. Matthew D. Lane,[1] and Gary S. Grest[1]
[1] *Sandia National Laboratories, Albuquerque, NM*

The high mechanical stiffness of single-nanoparticle thick membranes is believed to result from the local structure of ligand coatings that mediate interactions between nanoparticles. These ligand structures are not directly observable experimentally. We use molecular dynamics simulations to observe variations in ligand structure and simultaneously measure variations in membrane mechanical properties. We have shown previously that ligand end group has a large impact on ligand structure and membrane mechanical properties. Here we introduce and apply quantitative molecular structure measures to these membranes and extend analysis to multiple nanoparticle core sizes and ligand lengths. Simulations of nanoparticle membranes with nanoparticle core diameter 4 or 6 nm, ligand length 11 or 17 methylenes, and either carboxyl (COOH) or methyl (CH_3) ligand end groups are presented. In carboxyl-terminated ligand systems, structure and interactions are dominated by an end-to-end orientation of ligands. In methyl-terminated ligand systems large ordered ligand structures form, but nanoparticle interactions are dominated by disordered, partially-interdigitated ligands. Core size and ligand length also affect both ligand arrangement within the membrane and the membranes macroscopic mechanical response, but are secondary to the role of the ligand end group. Moreover, the particular end group (COOH or CH_3) alters the nature of how ligand length, in turn, affects the membrane properties. The effect of core size does not depend on ligand end group, with larger cores always leading to stiffer membranes. Asymmetry in the stress and ligand density is observed in membranes during preparation at a water-vapor interface, with the stress asymmetry persisting in all membranes after drying.

I. INTRODUCTION

Nanoparticles (NPs) made from metal cores coated with organic ligands are a common building block in a variety of nanoscale systems [1–3]. Membranes formed from nanoparticle (NP) monolayers have a number of properties such as controlled thickness and periodic structure, and mechanical strength and stiffness that make them useful in microscale sensor [4] and filtration [5–7] applications. Experiments have demonstrated a reproducible method for creating highly-ordered, single-NP thick membranes with a range of NP sizes and ligand types, from alkanethiols [8] to single-stranded DNA (ssDNA) [9]. Combining these reproducible fabrication methods with an understanding of the impact of nanostructure on mechanical properties could provide control over membrane properties. Experiments have studied variations in NP core and ligand type and their effects on membrane mechanical properties, but these experiments did not indicate clear nanoscale mechanisms for their mechanical stiffness [2, 10].

Nanoparticle membranes have been made with NPs composed of 4 - 13 nm diameter metal cores, commonly gold, coated with organic oligomers such as oleylamine or oleic acid [2, 8, 10]. In experiments, NPs are driven into a monolayer when a NP suspension wets a water droplet and the organic suspension fluid evaporates [10, 11]. Evaporation of the water droplet leaves a single NP-thick membrane on a silicon-nitride substrate. Micrometer size holes cut in the substrate create free-standing portions of the membrane which are up to tens of microns in size, and can be used to test the mechanical response. In experiments on ssDNA-coated NPs a similar but distinct process deposits a monolayer of NPs across microholes to form a membrane [9].

Mechanical properties of NP membranes are measured by either bulge or atomic force microscopy indentation testing. Young's moduli on the order 1 - 10 GPa have been measured for NP membranes with oligomer ligands such as poly allylamine hydrochloride [12], alkanethiol [2], or ssDNA ligands [9]. Measured elastic moduli vary with nanoparticle core size and ligand type. Both ligand chain interactions [2] and ligand end-group chemistry [13] are important in strengthening membranes and providing mechanical stability. Ligand binding strength has also been identified as determining membrane mechanical properties [2]. However, it can be difficult to determine experimentally whether variations in membrane stiffness are due to variations in controlled NP properties or uncontrolled sample variation. Similarly, it is difficult to determine the nanoscale mechanisms or structures that lead to different mechanical properties. Systematic measurements of membrane stiffness due to variation in NP core size, ligand length or end group have not been performed.

A number of molecular dynamics (MD) simulation studies have been performed measuring properties of ligands on single NPs and interactions between NPs. Simulations have generally utilized either fully-atomistic [14–20] or united atom force fields [21–30], and have looked at the effects of solvent [18, 23–25, 30], ligand end-group [15, 16, 20], and temperature [20–22] on ligand behavior. These studies show that end-group chemistry can influence NP solubility, for example end groups with higher polarity increase NP solubility in water. Simulations have also been used for detailed studies of interactions and ligand structure between two or three interacting NPs [27, 28, 31, 32]. These studies can provide some intuition about the ligand structure and NP interactions within many-NP assemblies. Assemblies of coated NPs and their formation have been studied using coarse-grained [33] and atomistic [19, 34] simulations in two and three dimensions.

Properties of three-dimensional NP crystals have been studied using coarse-grained [14, 35] and atomistic [36] models. These simulations have measured the superlattice mechanical properties [36] and found moduli of order 1-2 GPa, comparable to experimental results for three-dimensional nanocrystal supercrystals [1]. Previous simulations of two-dimensional membranes made from alkanethiol-coated NPs found membrane mechanical properties comparable to experiments, and indicated that ligand end-group chemistry can have a large effect on membrane mechanical properties [13].

Here we present MD studies of the ligand structure and mechanical properties of single-NP thick membranes for Au NPs with 4 or 6 nm core diameter. The ligand molecules investigated were $HS(CH_2)_{n-1}X$, where X is CH_3 or COOH and $n = 12$ or 18. These studies extend previous simulations to explore the effects of equilibration time and high-temperature annealing on ligand structure, confirming that simulations represent equilibrium ligand structures. Measurements of ligand density and stress indicate an asymmetry in dry membranes, imparted by the membrane formation at the water/vapor interface. Ligand atom neighbor statistics are used to quantify ligand structure. Structure measurements indicate that CH_3-terminated ligands on each NP orient to form ordered domains or bundles. Measurements also show that in regions of disorder between NPs some ligands interpenetrate. Pairwise interactions between interpenetrating ligand backbone atoms on neighboring NPs resist membrane deformation and increase membrane stiffness. In contrast to the interpenetration of CH_3-terminated ligands, COOH-terminated ligands orient end-to-end, and electrostatic interactions between end-group atoms increase membrane stiffness. Previous results showed the large influence of ligand end group on membrane mechanical properties in the case of 6 nm core diameter with $n = 12$ [13]. Measurements presented here confirm this finding and also show that variations in NP core diameter and ligand length change the membrane mechanical properties by modulating the extent of COOH end-end pairing or the CH_3 interpenetration. Our present MD studies allow us both to observe the effects of NP cores size and ligand length on the amount of ligand interpenetration and end-end pairing, and to correlate these effects with membrane mechanical stiffness.

Below we detail the different NP parameters and simulation methodology for testing mechanical properties and membrane lattice spacings. Measures of membrane asymmetry and mechanical properties are presented in Sec. III, as are measures of ligand structure.

II. METHODOLOGY

Nanoparticle preparation followed the procedure outlined in previous work [13, 17, 20]. Nanoparticle cores were either 4 or 6 nm in diameter, corresponding to about 2000 or 6700 Au atoms. [2]. Gold cores were cut from an FCC lattice, and were initially modeled with an embedded atom method potential [37]. Though we model the gold core explicitly, our results are consistent with previous simulations where the gold core was omitted [17, 34]. The temperature of the NP core was raised to 800 K for 1 ns to allow for some melting and softening of the NP edges and corners, and was then returned to 300 K. Following the NP core formation, Lennard-Jones (LJ) particles representing sulfur atoms were added to the simulation and adsorbed onto the gold core in order to create a random, uniform density of thiol binding sites. Experimentally, upon physisorption, the alkanethiol molecule binds to the Au nanoparticle through the sulfur head atom and loses the mercaptan hydrogen atom, transforming itself into an alkanethiolate. The density of the binding sites is governed by the LJ interaction parameters, which were chosen to match the experimental alkanethiol surface density of 4.7 $/\mathrm{nm}^2$ on a flat gold substrate [38–40]. These parameters produced 515 binding sites for 6 nm diameter and 260 sites on 4 nm diameter cores. Because the ligand surface density is high, the thiol mobility along the surface is very low. This allows us to treat the gold and sulfur atoms as a single rigid body. External forces exerted on each gold or sulfur atom are transmitted as forces or torques acting on the entire rigid body. Alkane chains initially oriented in the all-trans configuration were bonded to the sulfur atoms on the gold core surface.

Interactions between sulfur, carbon, hydrogen and oxygen atoms were modeled using the Optimized Potential for Liquid Simulations - All-Atom force field [41]. Atomic charges as well as nonbonded, bond, angle and dihedral interactions between atoms are all specified in this fully atomistic force field. Interactions between gold atoms and ligand atoms were modeled using a Buckingham potential [42]. Long-range electrostatic interactions were computed using the Particle-Particle-Particle-Mesh method with precision 3×10^{-5} [43]. The RESPA multistep integrator [44] was used to integrate bond, angle, dihedral and non-bonded interactions with a 1 fs time step and to integrate the long-range electrostatics with a 4 fs time step. Water molecules were simulated using the TIP4P/2005 model [45, 46] with H-O-H angles constrained via the SHAKE algorithm [47]. Simulations were thermostatted using a Langevin thermostat with time constant 0.1 ps to control the temperature. All simulations utilized the LAMMPS MD package [48].

Experimentally, NP membranes are formed when NPs are driven together at the liquid-vapor interface by evaporative surface area reduction and interparticle interactions [8]. We reproduce this formation process by replicating NPs in a 6×6 two-dimensional hexagonal lattice

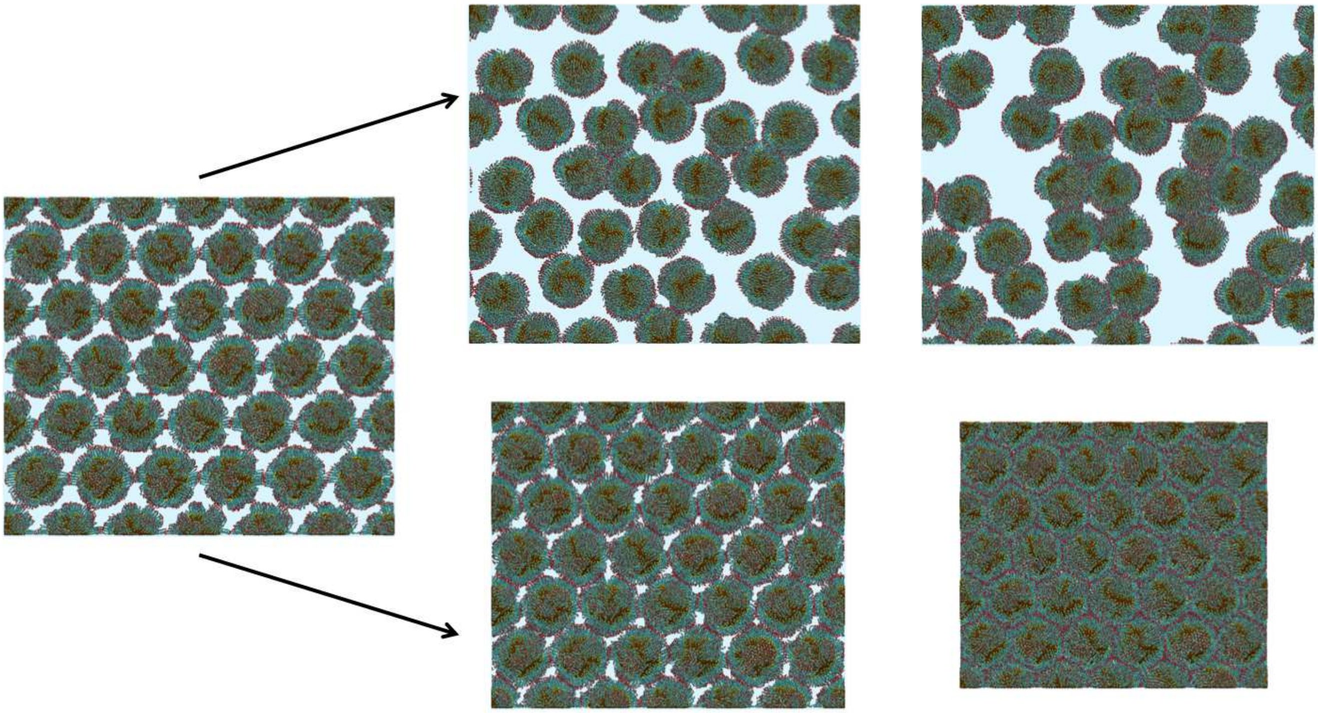

FIG. 1. (Color online) Top row: Configurations of NPs with 6 nm diameter cores and $n = 12$ COOH terminated ligands sampled at 10 ns and 50 ns during a free-particle simulation. Nanoparticles are placed at the liquid-vapor interface and are allowed to diffuse freely. Bottom row: The same NPs at the liquid-vapor interface undergoing isotropic compression. Water molecules are not shown.

as shown in Fig. 1 (a) and placing the array atop a $60.0 \times 60.0\sqrt{3}/2 \times 10$ nm water slab. A hexagonal lattice arrangement was chosen to match the experimentally observed NP configuration [2, 10]. Including outstretched ligands, the 6 nm NPs can be as much as 8 - 9 nm in diameter. An initial NP spacing $a_0 = 10.0$ nm was chosen so that the largest NPs, with 6 nm diameter and $n = 18$, were not touching. Simulations of cores held at large lattice spacing show the NP behavior in the dilute limit [17]. The simulation cell was periodic in all three directions, and the cell size in the z-direction was at least 30.0 nm, allowing for ample vacuum between the NPs and the second water-vapor interface. For some simulations NPs were placed on both the $+z$ and $-z$ air-water interfaces of the water slab for computational efficiency. The NP array and water samples combined were approximately two million atoms in size.

Simulations were run to measure whether NP aggregation for reasonable membrane sizes could be captured on the timescale of MD simulations. Simulations were run with no constraints or imposed deformations while NPs freely diffused at the water-vapor interface. Some simulations of this type were run for more than 55 ns. An example of the evolution of a NP array is shown in the top sequence of Fig. 1. NP configurations are shown at 10 ns and at 50 ns. NPs exhibit very slow movement after about 20 ns. Hence this approach to membrane formation is too slow to follow computationally. However, NPs exhibiting 2-fold or higher coordination give an initial estimate of the equilibrium membrane lattice constant. For 6 nm diameter NPs with $n = 12$ ligands the average spacing during free-NP simulations is 7.6 nm for COOH end groups and 7.5 nm for CH_3 end groups. Experiments have been performed for NPs with dodecanethiol ligands, and for these NPs the equilibrium spacing is in agreement [2, 10].

It is known from experiment that NPs of this size form membranes with long-range order with a hexagonal lattice [10]. We use a fixed isotropic compression to reproduce this long-range hexagonal order. Using the initial state with a 10.0 nm-spaced NP array and water, simulations were run with isotropic compression in the plane of the NPs. NP cores were kept rigid while the center of mass of each core was displaced to match the isotropic compression. NP cores were held fixed to a perfect hexagonal lattice and did not move in the lattice plane due to external forces, *ie* the net force on each NP core in the plane was set to zero throughout the isotropic compression. Atoms within the ligand and water molecules were displaced to match the imposed deformation. This procedure creates membrane configurations with a range of lattice constants. Ending states for the compressed array were chosen so that the NP spacing in the membranes matched the spacing determined from free-NP runs.

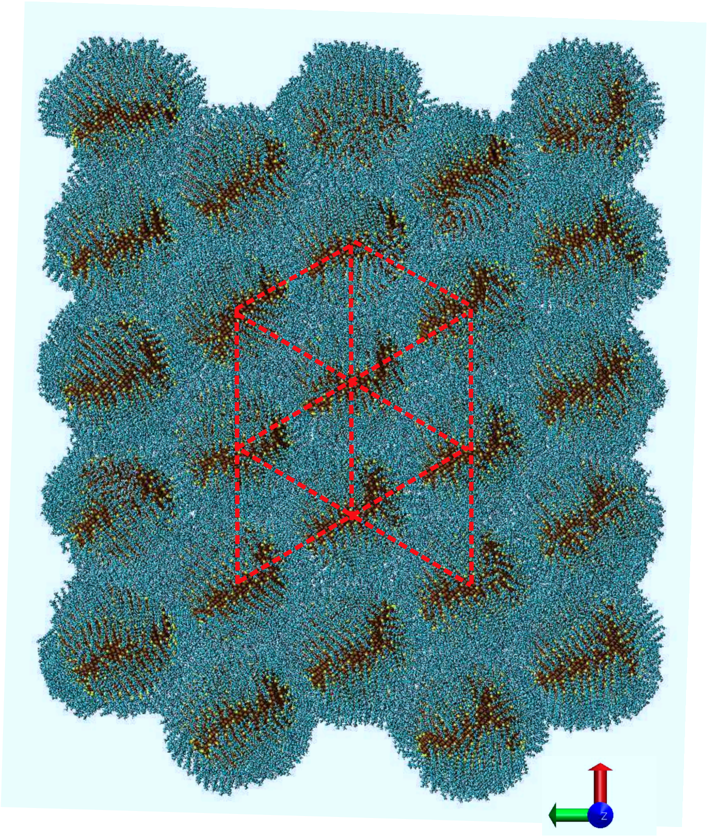

FIG. 2. (Color online) A 5×5 array of NPs with open boundary conditions for 6 nm diameter NPs with $n = 12$ CH_3-terminated ligands viewed from the vapor side. Dashed red lines show interior NPs used to determine lattice spacings.

After compression, dry NP membranes were formed via evaporation of the water. Following evaporation, membrane samples were equilibrated in vacuum for 5 - 20 ns. For some simulations the dried membrane configuration was replicated in the x or y directions (or both) in order to test for finite size effects. Previous results indicated negligible finite size effects for 6nm diameter cores with CH_3 and COOH-terminated ligands [13]. Dry membrane configurations can be made non-periodic by deleting NPs that span the periodic boundary and extending the simulation size in the membrane plane. This creates dry 5×5 NP membranes with open boundaries. All results below correspond to dry 6×6 periodic membrane samples except where explicitly stated.

The equilibrium lattice spacing for the dry membranes was measured using 5×5 NP membranes with open boundaries as shown in Fig. 2. Lattice spacings were calculated for NPs that have 6-fold coordination, *ie* not at the edges. Simulations of membranes with free boundaries began from well-equilibrated periodic samples that were simulated for at least 5 ns. The open samples started at lattice spacing near the final measured spacing, differing by up to 2% from the final determined lattice spacing. Measurements of NP lattice spacings are reported in Table I.

Dry periodic 6×6 NP membranes were then compressed to the lattice spacings found from simulations of free-edge samples for mechanical testing. Ultimately, the lattice spacings used for mechanical testing for all NP parameters were chosen to be at or near the free-edge membrane spacing result, and within a range where measurements of elastic constants were independent of the exact lattice spacing. Mechanical properties were measured by performing uniaxial extension and compression, biaxial extension and compression as well as pure shear on the dried membrane samples. Strain tests were performed at strain rates $\dot{\epsilon} = 5 \times 10^6$ s^{-1} or 5×10^5 s^{-1} corresponding to maximum velocities of about 0.3 - 3 m/s. For certain configurations results were compared with strain rate $\dot{\epsilon} = 5 \times 10^4$ s^{-1}.

An annealing sequence was implemented for the 6 nm NPs covered with $(CH_2)_{11}COOH$ and $(CH_2)_{11}CH_3$ ligands. This annealing was used to check that the states for mechanical testing are not history dependent. The membrane sample atop water was heated at constant area from 300 K to 400 K over 1 ns, held at 400 K for 2 ns, and then cooled from 400 K to 300 K over 1 ns. During the high temperature phase the ligands lose their local packing, which is restored as the temperature is reduced back to 300 K. Following the temperature cycle the water slab in the sample was removed to leave a dry, temperature-annealed sample. These dry temperature-annealed samples were then equilibrated for more than 10 ns for comparison with dry samples that were not annealed. We characterize the properties of dry membranes at elevated temperatures elsewhere [49].

Long equilibration runs were carried out for dry membranes with 6 nm core diameter and $n = 12$ COOH and CH_3-terminated ligands. These simulations ran for 20 ns and were used to estimate the time scale of ligand equilibration reported below. This in turn established the equilibration protocol for the other membrane samples. The samples reported in the results section were all equilibrated for at least 8 ns before mechanical testing. Measures of ligand interdigitation and end-group affinity near saturation over this period, indicating that the membranes are well equilibrated.

III. RESULTS

A. Membrane asymmetry

During membrane formation the membrane top is exposed to vacuum while the bottom is exposed to water. We measure the effect of these different environments on the ligand density and stress state. We measure the local stress within the dry membrane because a top-bottom asymmetry in the stress could explain previously observed spontaneous out-of-plane bending [50]. We also check whether the ligand inhomogeneity previously observed in the dilute limit [17, 20] persists as a top-bottom density asymmetry in dry membranes. We show below that the ligand density exhibits asymmetry

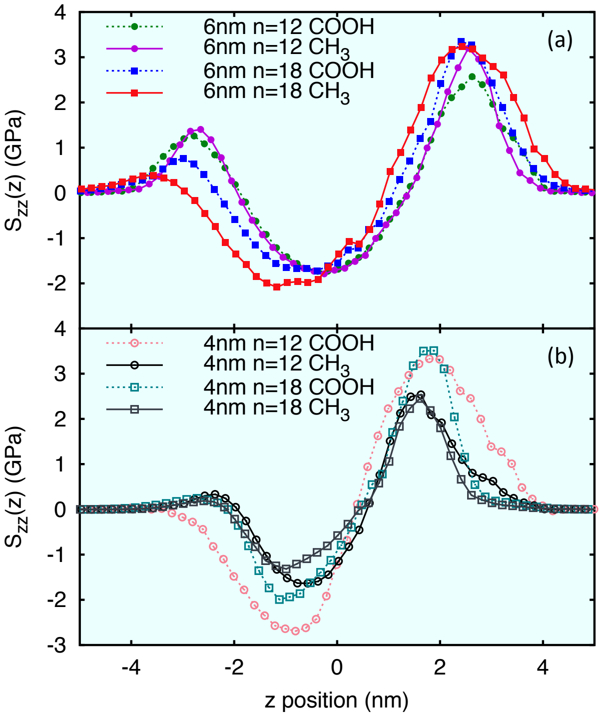

FIG. 3. (Color online) Stress $S_{zz}(z)$ for dry membrane samples with (a) 6 nm diameter NP cores and (b) 4 nm diameter NP cores with $n = 12$ or 18, COOH or CH_3 terminated ligands. The top of each membrane sample is oriented away from the water, in the positive z direction.

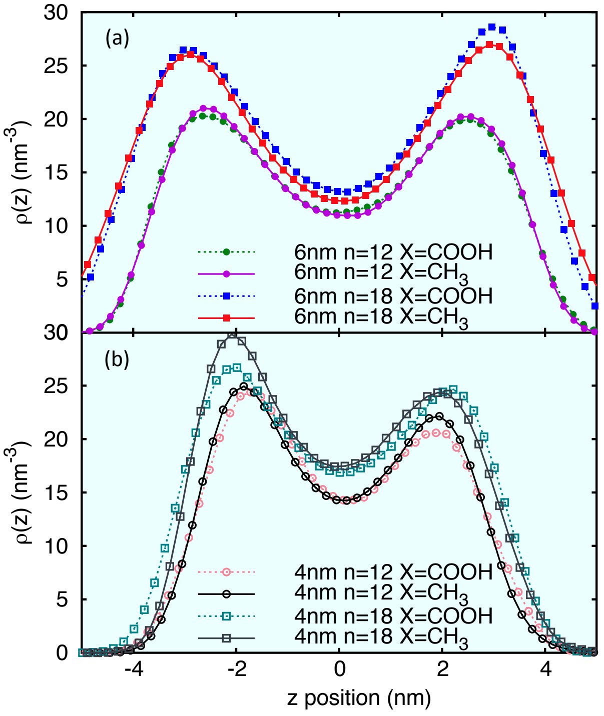

FIG. 4. (Color online) The ligand carbon number density as a function of height $\rho(z)$ through dry membrane samples with (a) 6 nm diameter NP cores and (b) 4 nm diameter cores.

only for NPs with high core curvature and long ligands, all membranes exhibit stress asymmetry.

We measure the stress as a function of height through the membrane. The stress S_{IJ} is given by the kinetic energy and virial contributions,

$$S_{IJ} \equiv V^{-1}\left[\sum_{i=1}^{N} m_i v_i^I v_i^J + \sum_{i=1}^{N}\sum_{j=1}^{N} F_{ij}^I r_{ij}^J\right] \qquad (1)$$

where I and J are the direction, v_i is the velocity of the ith particle and F_{ij} and r_{ij} are the force and distance between particles i and j [51]. N in the sum of particles corresponds to the volume V considered. Here we calculate S_{IJ} as a function of height z in slabs of width 0.2 nm which span the system in x and y.

Figure 3 (a) shows the S_{zz} component of stress as a function of height through the dry membranes with the equilibrium lattice spacing a_0. Positive regions in the curves demonstrate tension in the ligands while negative regions demonstrate compression. The figure shows compression near the membrane middle and tension away from the middle, with an asymmetry between the top and the bottom. Similar asymmetry is shown in Fig. 3 (b) for membranes with 4 nm diameter NP cores. All samples were equilibrated for 6 ns, and the stress profile changed little during this time. The top-bottom asymmetry in the tension indicates that the membrane would naturally roll toward the water layer if the edges were released. Indeed, we observe curvature of this type in our simulations of dry membranes with free edges, though our samples are too small to role. This top-bottom asymmetry in the stress could be related to experimental observations of out-of-plane bending [50].

One possible explanation for the asymmetric top-bottom stress state is a difference in ligand density due to the water/vapor environments. Figure 4 shows the density of ligand carbon atoms as a function of height through the membrane $\rho(z)$ for each of the membrane samples, with 6 nm core diameter membrane samples shown in (a) and 4 nm core samples in (b). The membranes show a high degree of top-bottom symmetry, ranging from essentially no asymmetry in the membrane with 6 nm core diameter and $n = 12$ CH_3-terminated ligands, to about 20% asymmetry in the membrane with 4 nm core diameter, $n = 18$, CH_3-terminated ligands. The evolution of the ligand density of these two membranes from the wet, dilute-NP state to the dry membrane state is charted in Fig. 5.

Figure 5 (a) shows the density of carbon atoms as a function of height through the membrane $\rho(z)$, for the membrane with 6 nm diameter cores and $n = 12$ CH_3 terminated ligands. The top-bottom asymmetry in the ligand density is pronounced for NPs in the dilute limit, obtained by holding NPs at lattice spacing 10 nm. As

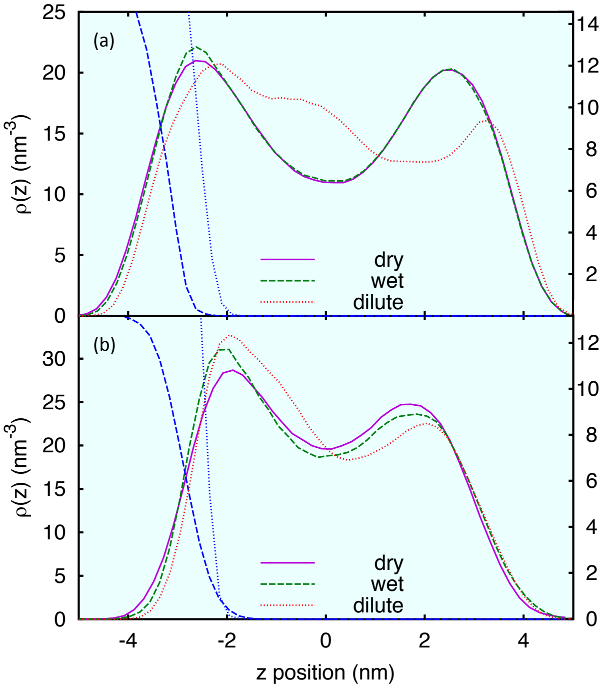

FIG. 5. (Color online) The ligand carbon number density as a function of height $\rho(z)$ through NPs with (a) 6 nm diameter core and $n = 12$ CH_3 terminated ligands and (b) 4 nm diameter core and $n = 18$ CH_3 terminated ligands. In the dilute case NPs are not touching and axes for these data are on the right. Blue dotted and dashed density curves indicate the water density in the dilute and wet case respectively.

the lattice spacing is reduced the density asymmetry is also reduced. At the equilibrium lattice spacing there is a slight asymmetry in the ligand density on water that disappears when the membrane is dried.

Figure 5 (b) shows $\rho(z)$ for 4 nm diameter core NPs with $n = 18$ CH_3 terminated ligands. As has been found previously, NPs with smaller core diameters and longer ligands display more pronounced ligand inhomogeneity[17, 19]. For NPs with 4 nm core diameter and $n = 18$, CH_3-terminated ligands, the density asymmetry is reduced, but persists in the dry membrane. The asymmetry in the peak height for this membrane is about 20% and is the largest observed for our dry membranes. The asymmetry in the dry membrane reflects the larger inhomogeneity observed in the dilute limit due to larger NP curvature and stronger local ligand order.

The top-bottom asymmetry in the density and stress provide an interesting contrast. While the stress asymmetry persists in the dry membrane for all samples, the density asymmetry depends on NP parameters. The inhomogeneity in the ligand density is consistent with previous studies, where smaller NP cores with longer ligands exhibit greater inhomogeneity [17, 20]. Independent of the ligand density, a strong asymmetry is observed in the membrane stress, imparted by the water-vapor environment during formation.

B. Membrane mechanical properties

Mechanical testing allows us to correlate NP membrane mechanical response with NP properties and ligand structural details. Ideally, we would both compare with the experimental Young's modulus and use the experimental deformation geometry [2]. The experimental deformation geometry is most closely matched in simulation using biaxial extension, which induces an areal expansion. However, this deformation geometry does not uniquely determine the Young's modulus or Poisson ratio. Hence, we also make measurements using uniaxial extension and compression, and pure-shear deformation geometries. Mechanical testing is performed on each of the membrane samples, and for dodecanethiol ligands the measured Young's modulus values are consistent with those measured in experiment. Measurements of membrane moduli are consistent with our previous finding that ligand end group can dramatically alter membrane mechanical properties. Further, NP core size also strongly influences membrane stiffness.

Figure 6 shows the stress-strain response of the 4 nm and 6 nm diameter $n = 12$ COOH and CH_3 membranes undergoing pure shear. The stress corresponds to the stress for the entire system, but has been multiplied by the simulation box height to produce a two-dimensional stress [13]. The two-dimensional shear modulus may be read from the plot as the slope of the stress-strain curve. The data show two significant features: larger NPs produce stiffer membranes, as do COOH end groups. The ligand structural properties related to these features are explored below.

The Poisson ratio and three-dimensional Young's modulus, formed by dividing the two-dimensional modulus by the membrane height h, are recorded in Table I for each NP core size and ligand configuration. Values for the Poisson ratio are calculated from the uniaxial deformation geometry. In this geometry the sample is deformed in one dimension, with the other dimension held fixed. The stress response of the material in each dimension allows one to calculate both the Young's modulus and Poisson ratio. Values for the Young's modulus recorded in Table I are calculated from the stress response during biaxial extension simulations. This geometry most closely matches that used in experiments, but measurements of the Poisson ratio from the uniaxial geometry are required to calculate the Young's modulus. Young's modulus and Poisson ratio calculated from different deformation geometries vary by 10-20%, which we take as the uncertainty in our measurements. All values of the Poisson ratio fall within this uncertainty around a value of 0.3, which is common to many materials. This value matches the one assumed in previous experimental analysis [2].

We have performed a number of tests to check that there is no influence of strain-rate or boundary effects in our results. We confirm that there is no viscous response by holding a membrane for 0.5 ns after applying a 2%

TABLE I. Equilibrium height h, average and standard deviation of lattice spacing a_0 and $\langle \delta a_0^2 \rangle^{\frac{1}{2}}$, modulus E and Poisson ratio ν for dry membranes as a function of core diameter, ligand length, and end group.

Diameter (nm)	Length $n =$	End X=	h (nm)	$\langle a_0 \rangle$ (nm)	$\langle \delta a_0^2 \rangle^{\frac{1}{2}}$ (nm)	E (GPa)	ν
6.0	12	CH_3	7.6	7.5	0.11	1.5	0.34
6.0	18	CH_3	8.7	7.7	0.18	2.3	0.30
4.0	12	CH_3	5.8	5.6	0.09	0.8	0.34
4.0	18	CH_3	7.0	6.1	0.25	0.7	0.28
6.0	12	COOH	7.6	7.6	0.14	3.6	0.27
6.0	18	COOH	8.6	7.7	0.09	3.5	0.29
4.0	12	COOH	6.2	5.6	0.09	1.8	0.33
4.0	18	COOH	6.3	6.1	0.17	0.9	0.32

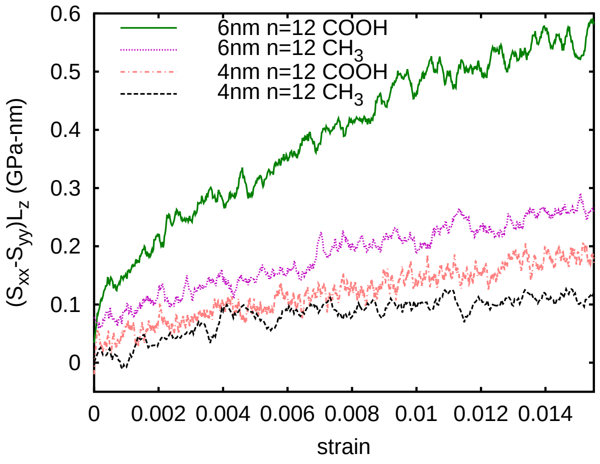

FIG. 6. (Color online) Typical stress-strain curves for samples undergoing pure shear deformation. Data for 6 nm diameter cores from Ref. [13] are shown to contrast with the 4 nm core-diameter data.

strain. Over this period the stress recovers at most 5% of the applied stress, well within the noise of the data. We also implemented an alternate deformation protocol on a membrane with strain applied in one periodic direction while the transverse direction had a free boundary condition. For different NP parameters membranes show a stiffness consistent with the Young's modulus reported in Table 1.

The system with $n = 12$ COOH terminated ligands shown in Fig. 6 has the highest Young's modulus of the systems, $E = 3.6$ GPa. The membrane with $n = 12$ methyl-terminated ligands is substantially weaker with $E = 1.5$ GPa. This difference in stiffness is reflected in Fig. 6. In experiments, Young's moduli can range from 1 - 14 GPa [2], with an average value $E = 4$ GPa for 5 nm diameter cores with dodecanethiol ligands. For such a wide range of measurements error bars are greater than 4 GPa, however these measurements are the same order of magnitude as ours [52].

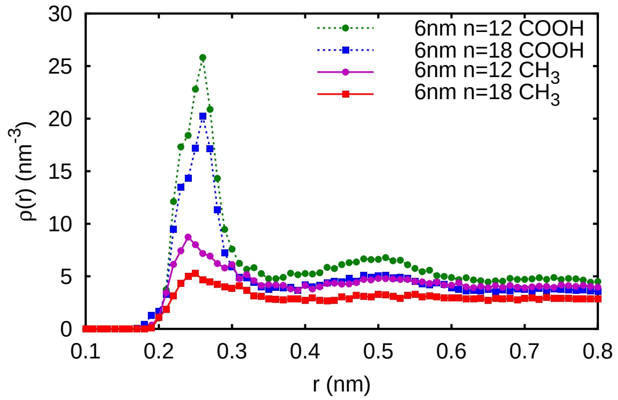

FIG. 7. (Color online) The radial density function $\rho(r)$ for end-group carbon atoms on differing NPs for different chain length and end group. Curves for different NP diameters are similar. Data for $n = 12$ from Ref. [13] are shown to contrast with the $n = 18$ case.

C. End-group affinity

The significantly higher moduli for membranes with COOH-terminated ligands indicate that ligand end group influences mechanical properties. One important difference between methyl and carboxyl end groups is the strength of electrostatic interactions. Charge separation between oxygen and hydrogen atoms leads to hydrogen bonding between COOH groups, e.g. dimers of carboxylic acid. This affinity between COOH end groups influences ligand structure. We directly contrast ligand structures for carboxyl and methyl terminated ligands through the end-carbon radial density function.

To compare the end-group affinity between terminal groups we measure the radial density function $\rho(r)$, which is formed from a histogram of distances between an end-group carbon on one NP and the end-group carbons on surrounding NPs. A comparison of $\rho(r)$ for 6 nm $n = 12$ and $n = 18$ COOH and CH_3 membranes is shown in Fig. 7. The most striking feature in Fig. 7 is the contrast in the density peak for the different end-groups. The electrostatic attraction between charges in the COOH groups causes ligands to form an end-to-end structure, indicating very little interdigitation in these systems. In contrast, CH_3 end-groups do not show a strong affinity for one another. The increased affinity between COOH end groups relative to CH_3 is evident in the ligand structure and accounts for the increased stiffness of membranes with these end groups. It is also clear in Fig. 7 that the end-group affinity is reduced for longer ligands, possibly explaining the feature of decreasing stiffness with increasing chain length observed in Table I for COOH end groups.

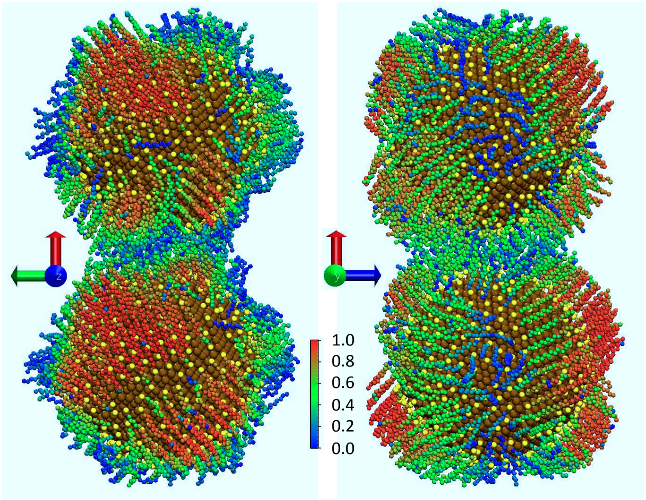

FIG. 8. (Color online) A snapshot of ligands on adjacent NPs at 300 K for 6 nm diameter NPs with $n = 12$ CH_3 terminated ligands taken from a 6×6 membrane on water. Ligand carbon atoms are colored according to the p_2 measure of local order. The left snapshot shows the atoms from the membrane top-view. On the right the axes have been rotated by 90° to show the band of disordered ligands corresponding to the membrane plane.

D. Ligand order

In addition to end group interactions, another possible source of stiffness or mechanical strength is the interdigitation of ordered ligand regions. At room temperature alkane oligomers on NPs form regions of ordered bundles due to interaction with a poor solvent [20]. Bundle structures could form strong bonds between adjacent NPs if ordered regions interdigitated strongly. We examine ligand order and do not find this type of structure.

A comparison of two NPs taken from a 6×6 membrane with CH_3 terminated ligands atop water at 300 K is shown in Fig. 8. Ligand carbon atoms are colored according to the local order measure

$$p_2(i) = \frac{1}{2}\langle 3\cos^2\theta_{ij} - 1\rangle_j. \qquad (2)$$

For each carbon atom i, $p_2(i)$ is averaged over carbon atoms j within a cutoff radius and θ_{ij} is the angle formed by the vectors between carbon atoms $i-1$ and $i+1$ and carbon atoms $j-1$ and $j+1$. In Fig. 8 the snapshot on the left views the NPs from above the membrane and shows large regions of ordered ligands. On the right the view has been rotated 90° to expose the membrane cross-section. Regions of disordered ligands coincide with the positions of neighbor NPs.

These contrasting views indicate that there are large ordered ligand regions within membranes but that these regions do not occur between neighboring NPs. Thus, ligand atoms that mediate NP interactions are found within regions with low order or at the boundaries of ordered regions. Ligand structures and interactions in the observed low-order regions are less stable and weaker than within highly ordered regions. This modifies the previous view that ordered, interdigitated alkane chains are the source of high strength and stiffness within membranes.

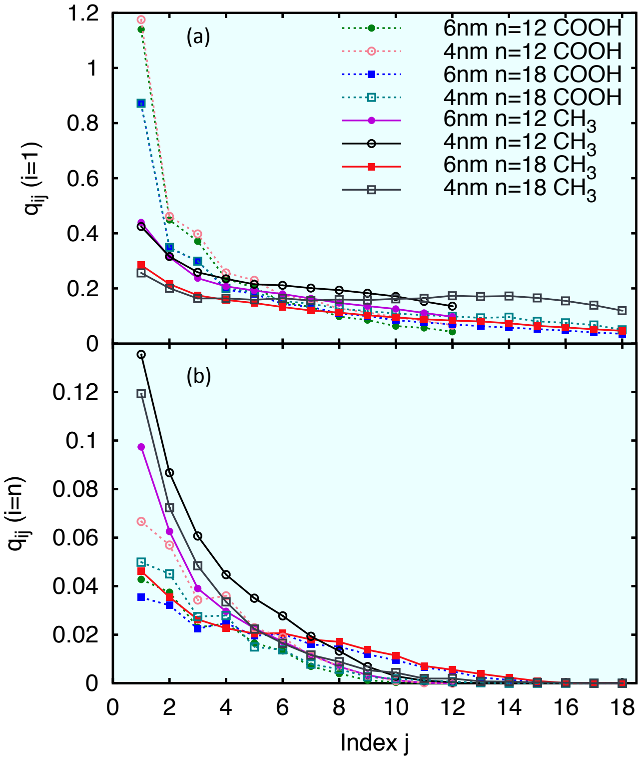

FIG. 9. (a) (Color online) The normalized number of neighbors q_{ij} with $i = 1$ for dry membranes with different NP diameter and ligand chain length n. (b) The normalized number of neighbors with $i = n$ for the same NP configurations.

E. Ligand structure

Previously we used visual analysis and proxy quantities such as end-group affinity to assess the extent and end-group dependence of ligand structure [13]. Here we study ligand structure directly and report results for a number of different NP parameters as well as for different system preparation and equilibration protocols. The importance of end-end interactions for COOH end groups is reiterated. Some interpenetration of CH_3 terminated ligands is observed. Interpenetration of CH_3-terminated ligands and end-group pairing of COOH-terminated ligands are correlated with membrane stiffness.

One measure of ligand structure is the number of ligand atom neighbors from adjacent nanoparticles. In particular, the position of each atom and its neighbors along their respective ligands indicates how much ligand atoms from adjacent NPs contact, and to what extent the ligands interpenetrate. If we label ligand carbon atoms with an index i from $1 \to n$, where $i = n$ is the innermost carbon and $i = 1$ is in the end-group, then we can measure ligand structure using the number of neighbors with backbone index j for all carbons with index i

$$q_{ij} = N_L^{-1}\left(\sum_{k,l\neq k}\sum_{m,n}\theta(r_c - |\vec{r}_{ikm} - \vec{r}_{jln}|)\right) \qquad (3)$$

where $\theta(x)$ is the Heaviside step function. The sums on k and l are over the NP index while the sums on n and m are over the ligands on each NP so that the vector $\vec{r}_{ikm}$ represents the carbon atom in the ith position along the mth ligand on the kth NP. The normalization factor N_L is the total number of ligands. The neighbor radial cutoff $r_c = 0.5$ nm is chosen, but results are qualitatively insensitive to the cutoff. Indices with particular importance are $i = n$ and $i = 1$, since these give information about the innermost and end-group carbon atoms, respectively.

Figure 9 shows q_{ij} for (a) $i = 1$ and (b) $i = n$ for different NP diameter, ligand length, and end group in dry membrane samples. In Fig. 9 (a) for all chain lengths and NP diameters, the $i = j = 1$ carbons have about three times as many neighbors for COOH as for CH_3. This indicates the COOH end groups are paired where the CH_3 are not. In contrast, in Fig. 9(b) for $i = n$, the peak value at $j = 1$ is much higher for CH_3 end groups, about twice as high as for COOH end groups, albeit at much lower absolute value than the $i = j = 1$ case. This indicates that CH_3 terminated ligands are more likely to interpenetrate and not orient end-to-end.

The influence of NP core size on membrane properties is evident in the ligand structural properties for both COOH and CH_3 terminated ligands. For COOH terminated ligands the coincident curves for 4 and 6 nm core diameters in Fig. 9 (a) explain the variation in membrane stiffness with core size. Since q_{ij} is normalized by the total number of ligands, the coincident curves indicate that 4 nm diameter NP cores have half as many COOH-COOH interactions per NP as the 6 nm diameter NP cores due to the different core surface areas. This corresponds directly with the ≈50% decrease in stiffness for membranes with 4 nm relative to 6 nm diameter NP cores. For CH_3 terminated ligands the same effect occurs, but is weaker. In Fig. 9 (b), q_{ij} for $i = n$ shown shows an increase for the 4 nm core diameter vs the 6 nm diameter, indicating increasing ligand interpenetration. However the total number of neighbors decreases due to the normalization. This decrease in ligand interactions corresponds to a reduction in stiffness for 4nm diameter NP cores as compared to 6 nm core diameters. Though the effect of NP core size is stronger for COOH than for CH_3 end groups the overall number of ligand interactions, governed by the core-diameter, is important for both.

Variations in ligand structure with length n also correlate with the membrane mechanical properties for both end-group types. For COOH end-groups a decrease of 25% in q_{ij} with $i = j = 1$ for $n = 18$ ligands relative to $n = 12$ is shown in Fig. 9 (a). This matches closely the decrease in stiffness for membranes with $n = 18$ vs $n = 12$ COOH terminated ligands. The effect of ligand length on membrane stiffness is less clear for CH_3 terminated ligands. There is a slower, more linear decay with j for q_{ij} for $i = n$ in Fig. 9 (b) for the 6 nm cores with $n = 18$ CH_3 terminated ligands. This form indicates higher interpenetration for atoms along the ligand, and correlates with increased membrane stiffness. For 4 nm cores this increased interpenetration for longer ligands is not seen, and the result is the least-stiff membrane measured. This contrast implies that both NP core curvature and ligand length influence ligand interpenetration for CH_3 terminated ligands.

Different physical mechanisms for membrane stability are highlighted by q_{ij} for ligands with COOH vs. CH_3 end groups. For ligands with COOH end groups, the importance of COOH-COOH affinity and hydrogen bonding is confirmed. The number of end-carbon pairs directly explains the variation in membrane mechanical properties with NP core size and ligand length. Results for q_{ij} show that for CH_3 terminated ligands interpenetration and interactions between carbon atoms along ligands provide mechanical stability. For CH_3 terminated ligands 6 nm cores produce stiffer membranes, indicating that the absolute number of interactions is also important for these ligands. Interpenetration is highest for longer CH_3-terminated ligands on 6 nm diameter cores, but is not increased for $n = 18$ ligands relative to $n = 12$ on 4 nm diameter cores. This indicates that ligand length and core curvature both play a role in determining the interpenetration of CH_3 terminated ligands. Interpenetration of CH_3 ligands is correlated with membrane stiffness.

F. Ligand structure equilibration and stability

Our aim was to measure equilibrium, static membrane and ligand properties. The interactions and structures both along ligands and between end groups evolve during membrane formation and equilibration. We have quantified this evolution through measures of q_{ij} and show that these quantities do not evolve in the equilibrium membrane state. Further, through a thermal-annealing process we have checked that ligand and membrane properties are independent of thermal history. We compare a membrane sample that has been heated to 400 K with one that does not undergo annealing. Both samples have been equilibrated for 8 ns. Important ligand structural features are disrupted during thermal annealing, however each of the important ligand structures measured above, ligand order, backbone or end-group interactions re-form or recover after thermal annealing.

The extent of ligand and end-group structural evolution is illustrated using long-time equilibration of 6 nm diameter core $n = 12$ dry membranes. Figure 10 (a) shows q_{ij} for $i = j = 1$ over 18 ns. After increasing ≈40% over 5 ns the quantity saturates over the next 10 ns, increasing by 10%. Figure 10 (b) shows $\sum_j q_{ij}$ for $i = 12$. Time $t = 0$ corresponds to the time when wa-

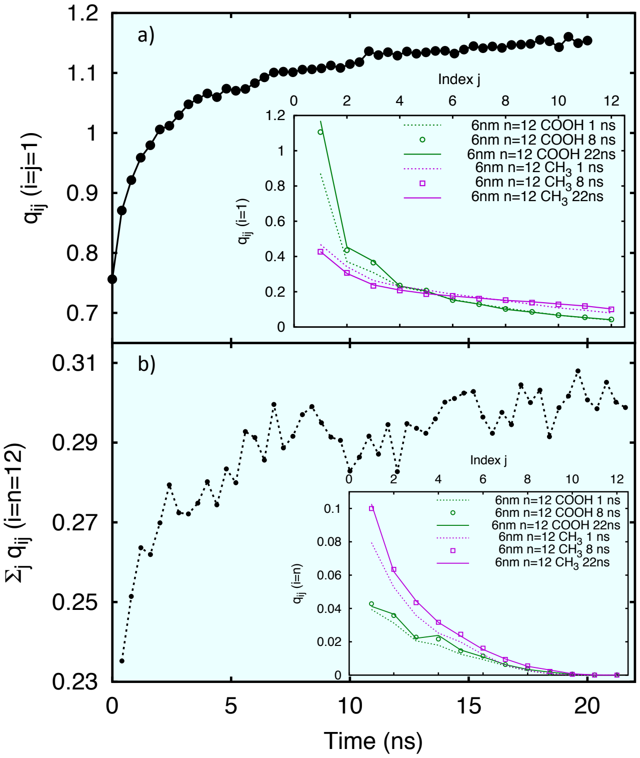

FIG. 10. (Color online) (a) q_{ij} for $i = j = 1$ for the 6 nm diameter $n = 12$ COOH end group system and (b) $\sum_j q_{ij}$ for $i = 12$ for the 6 nm $n = 12$ CH_3 end group system as a function of time since membrane formation and drying. Inset are the full histograms of q_{ij} for a) $i = 1$ and b) $i = 12$ for the 6nm diameter $n = 12$ NP systems taken at 1, 8, and 22 ns.

ter is removed following the compression of the NPs to the equilibrium membrane lattice spacing. After a rapid increase of ≈20% between 0 - 5 ns the value saturates between 5 - 10 ns. These results indicate that for both quantities the majority of structure forms in the first 5 ns following or during membrane formation, with minor evolution over the next 5 - 10 ns. Histograms of q_{ij} for 6nm $n = 12$ NP systems taken at 1, 8, and 22 ns shown in the inset demonstrate that the q_{ij} measure changes dramatically between 1 and 8 ns, with minor changes between 8 and 22 ns. This time scale motivates our choice to measure ligand structure and membrane mechanical response after 8 ns of equilibration. Values for both quantities increase slightly after 8 ns, however we choose this time as a balance between full equilibration and computational expense.

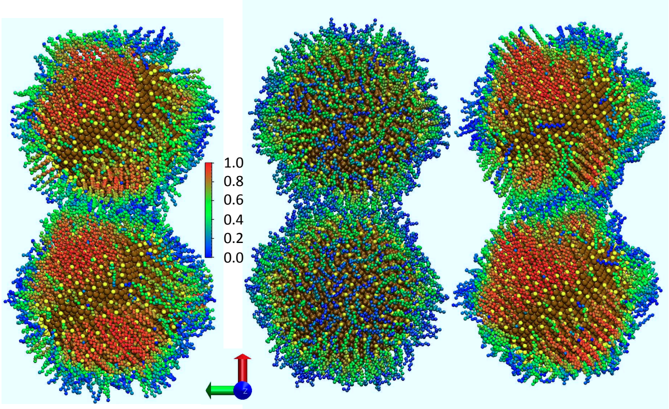

FIG. 11. (Color online) A snapshot of ligands on adjacent NPs at 300 K before annealing (left), 400 K (middle) and 300 K after annealing (right) for 6 nm diameter NPs with $n = 12$ CH_3 terminated ligands taken from a 6×6 membrane on water. Ligand carbon atoms are colored according to the p_2 measure of local order.

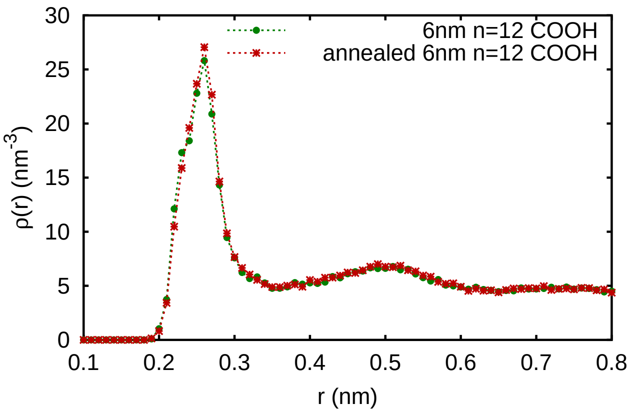

FIG. 12. (Color online) The radial density function $\rho(r)$ for 6 nm diameter $n = 12$ COOH terminated ligand membranes that have or have not undergone thermal annealing. In both cases membranes are dry and have been equilibrated for at least 8 ns.

At increased temperature ligand structures are changed dramatically, in particular the p_2 measure of ligand ordering. Fig. 11 shows two NPs taken from a 6×6 membrane with CH_3 terminated ligands atop water at 300 K (left) and 400 K (middle) and after annealing at 300 K (right). As in Fig. 8, carbon atoms are colored according to the local order measure $p_2(i)$. Not only are the 300 K samples visually similar, but the distribution of p_2 values are comparable between the two samples. Thus, thermal annealing appears to completely reset ligand ordering, yet bundle structures reform after thermal annealing.

The effect of COOH end-group interactions on ligand structure is strong for membranes that undergo annealing. Figure 12 shows $\rho(r)$ for $n = 12$ chains on 6 nm diameter NPs, comparing the effects of high-temperature annealing on end-group structure. The peak densities in $\rho(r)$ for COOH-terminated ligands are comparable before and after annealing. Independent of thermal history, COOH end-groups form end-to-end structures and this state represents an equilibrium structure.

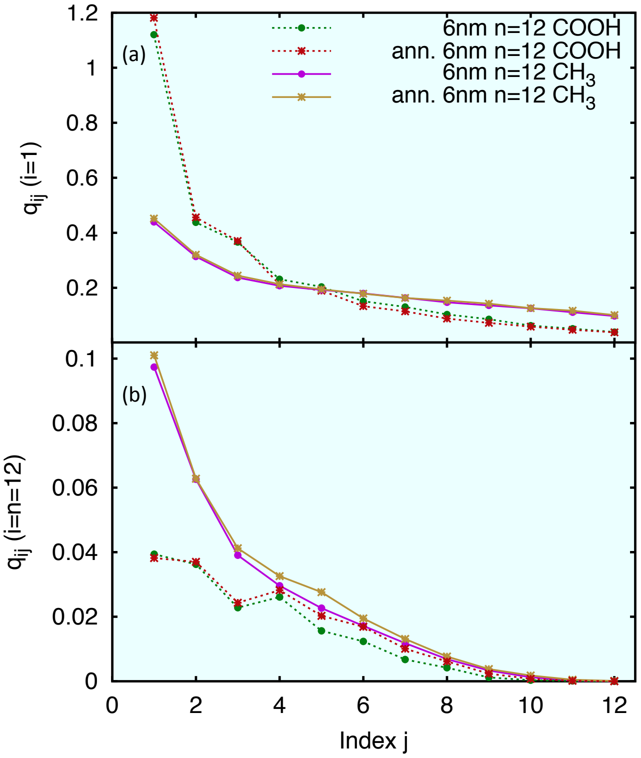

FIG. 13. (a) (Color online) The normalized number of neighbors q_{ij} for backbone index $i = 1$ for 6 nm diameter, $n = 12$ dry membrane samples with and without thermal annealing. (b) The same membrane samples for backbone index $i = 12$.

Also of interest is the effect of thermal annealing on q_{ij}. We detail elsewhere the weakening of ligand end group and ligand backbone structure with increased temperature [49]. Here we compare ligand end-group and backbone structure before and after thermal annealing. Figure 13 (a) shows q_{ij} for $i = 1$ for both the 6 nm diameter, $n = 12$ COOH and CH_3 membranes before and after annealing. The COOH end-groups have a similar end-to-end structure before and after thermal annealing, indicating, as before, that high-temperature annealing does not permanently alter the end-group structures. The $i = 12$ case for q_{ij} is shown in Fig. 13 (b). The ligand neighbors of the CH_3 terminated ligands are comparable before and after the thermal annealing, indicating that although ligand structures are altered during thermal annealing, these structures fully recover afterward.

IV. CONCLUSIONS

Molecular dynamics simulations provide measurements of nanoscale structural features within NP membranes while reproducing macroscopic features. Nanoscale features such as ligand order, ligand atom neighbors, ligand density, local stress and end-group pairing are all accessible through MD. Measurements of these quantities provide insight into nanoscale details underlying the macroscopic properties measured for these NP membranes.

Both the ligand density and local stress exhibit a membrane top-bottom asymmetry induced by the membrane formation process at the liquid-vapor interface. In the dilute limit the ligand density asymmetry is large for all NP core-ligand combinations. This asymmetry persists in the dry membrane state for NPs with high core curvature and longer ligands, but completely disappears for larger NP cores with shorter ligands. In contrast, the membrane stress-asymmetry persists in the dry-membrane state for all membrane samples.

Ligands display order and bundling at 300 K due to interactions with water or vacuum. Measurements of the $p_2(i)$ local order parameter indicate that large regions of ligand order exist on areas of NPs that coincide with the membrane top and bottom. In contrast, regions of disorder occur within the membrane plane, indicating that regions where ligands from neighboring NPs interact are largely disordered.

Ligand end-group and backbone structures differ dramatically for COOH and CH_3 end groups. Electrostatic interactions produce an end-group affinity that is observed in the radial density function $\rho(r)$ for COOH end groups but not for CH_3 end groups. The same COOH end-group pairing is visible in measures of neighbors for end-group atoms in q_{ij} for $i = 1$. In contrast, the CH_3 ligands exhibit higher interpenetration, seen in q_{ij} for $i = n$.

Molecular dynamics simulations allow simultaneous measurement of macroscopic quantities such as elastic constants and nanoscale ligand structural features. Measurements of ligand neighbor statistics for different NP configurations indicate that increased ligand interpenetration (for CH_3) or end-end pairing (for COOH) produce stiffer membranes. Membranes with COOH-terminated ligands are stiffer due to end-group pairing and electrostatic interactions. Membrane stiffness decreases with decreasing NP core size for both end groups. Individual end-group pairs for COOH groups have the same strength for 4 nm and 6 nm core diameter NPs. However a 50% decrease in the number of end-group interactions for 4 nm diameter cores correlates with a 50% decrease in membrane stiffness. A similar but smaller effect exists for CH_3 terminated ligands, resulting in a decrease in membrane stiffness for smaller NP core size.

Variations in ligand structure with ligand length also correlate with membrane stiffness measurements. For COOH-terminated ligands, a decrease in membrane stiffness for $n = 18$ relative to $n = 12$ corresponds to a decrease in COOH pairing measured in both $\rho(r)$ and q_{ij} for $i = 1$. For CH_3-terminated ligands, q_{ij} for $i = n$ shown in Fig. 9 shows that longer $n = 18$ ligands interpenetrate more relative to $n = 12$ for 6 nm but not for 4 nm diameter cores, indicating that ligand interdigitation depends on both NP core curvature as well as ligand length.

Measures of ligand structure during long-time equilibration and after thermal annealing indicate that measured ligand structures represent equilibrium states.

Measures of end-group and ligand structure indicate that ligand structure is largely formed during or in the first 5 ns after membrane formation and that values reach steady state between 5 - 10 ns. After thermal annealing NP ligand structures reform to match those before annealing. Measures of ligand order, interpenetration and end-group pairing all are indistinguishable before and after thermal annealing, even though ligand structure is largely disrupted at 400 K.

Simulations provide the ability to simultaneously probe nanoscale detail and bulk mechanical properties. While membrane mechanical properties match those found in experiments, nanoscale details indicate significant differences in ligand structure and interactions that depend on end-group. These differences account for significant variations in bulk mechanical properties. These insights could allow for increased control over ligand conformation and interactions and ultimately membrane properties.

ACKNOWLEDGEMENTS

We thank X.-M. Lin and H. Jaeger for helpful discussions. Research was carried out in part, at the Center for Integrated Nanotechnologies, a U.S. Department of Energy, Office of Basic Energy Sciences user facility. Sandia National Laboratories is a multi-program laboratory managed and operated by Sandia Corporation, a wholly owned subsidiary of Lockheed Martin Corporation, for the U.S. Department of Energy's National Nuclear Security Administration under contract DE-AC04-94AL85000.

---

[1] E. Tam, P. Podsiadlo, E. Shevchenko, D. F. Ogletree, M.-P. Delplancke-Ogletree, and P. D. Ashby, Nano Lett. **10**, 2363 (2010).
[2] J. He, P. Kanjanaboos, N. L. Frazer, A. Weis, X.-M. Lin, and H. M. Jaeger, Small **6**, 1449 (2010).
[3] H. Wu, F. Bai, Z. Sun, R. E. Haddad, D. M. Boye, Z. Wang, and H. Fan, Angew. Chimie Intl. Ed. **49**, 8431 (2010).
[4] C. Jiang, S. Markutsya, Y. Pikus, and V. V. Tsukruk, Nat. Mater. **3**, 721 (2004).
[5] C. C. Striemer, T. R. Gaborski, J. L. McGrath, and P. M. Fauchet, Nature **445**, 749 (2007).
[6] E. Barry, S. P. McBride, H. M. Jaeger, and X.-M. Lin, Nat Commun **5** (2014).
[7] J. He, X.-M. Lin, H. Chan, L. Vukovic, P. Kral, and H. M. Jaeger, Nano Lett **11**, 2430 (2011).
[8] T. P. Bigioni, X.-M. Lin, T. T. Nguyen, E. I. Corwin, T. A. Witten, and H. M. Jaeger, Nat. Mater. **5**, 265 (2006).
[9] W. Cheng, M. J. Campolongo, J. J. Cha, S. J. Tan, C. C. Umbach, D. A. Muller, and D. Luo, Nat. Mater. **8**, 519 (2009).
[10] K. E. Mueggenburg, X.-M. Lin, R. H. Goldsmith, and H. M. Jaeger, Nat. Mater. **6**, 656 (2007).
[11] C. P. Joshi, Y. Shim, T. P. Bigioni, and J. G. Amar, Phys. Rev. E **90**, 032406 (2014).
[12] S. Markutsya, C. Jiang, Y. Pikus, and V. Tsukruk, Adv. Func. Mater. **15**, 771 (2005).
[13] K. M. Salerno, D. S. Bolintineanu, J. M. D. Lane, and G. S. Grest, Phys. Rev. Lett. **113**, 258301 (2014).
[14] A. P. Kaushik and P. Clancy, J. Chem. Phys. **136**, 114702 (2012).
[15] A.-C. Yang and C.-I. Weng, J. Phys. Chem. C **114**, 8697 (2010).
[16] A.-C. Yang, C.-I. Weng, and T.-C. Chen, J. Chem. Phys. **135**, 034101 (2011).
[17] J. M. D. Lane and G. S. Grest, Phys. Rev. Lett. **104**, 235501 (2010).
[18] B. L. Peters, J. M. D. Lane, A. E. Ismail, and G. S. Grest, Langmuir **28**, 17443 (2012).
[19] J. M. D. Lane and G. S. Grest, Nanoscale **6**, 5132 (2014).
[20] D. S. Bolintineanu, J. M. D. Lane, and G. S. Grest, Langmuir **30**, 11075 (2014).
[21] P. K. Ghorai and S. C. Glotzer, J. Phys. Chem. C **111**, 15857 (2007).
[22] W. D. Luedtke and U. Landman, J. Phys. Chem. B **102**, 6566 (1998).
[23] K. A. Tay and F. Bresme, J. Am. Chem. Soc. **128**, 14166 (2006).
[24] M. Lal, M. Plummer, N. J. Richmond, and W. Smith, J. Phys. Chem. B **108**, 6052 (2004).
[25] R. Pool, P. Schapotschnikow, and T. J. H. Vlugt, J. Phys. Chem. C **111**, 10201 (2007).
[26] N. Patel and S. A. Egorov, J. Chem. Phys. **126**, 054706 (2007).
[27] P. Schapotschnikow and T. J. H. Vlugt, J. Chem. Phys. **131**, 124705 (2009).
[28] P. Schapotschnikow, R. Pool, and T. J. H. Vlugt, Nano Lett. **8**, 2930 (2008).
[29] A. P. Kaushik and P. Clancy, J. Comput. Chem. **34**, 523 (2013).
[30] A. Widmer-Cooper and P. Geissler, Nano Lett. **14**, 57 (2014).
[31] B. J. Henz, P. W. Chung, J. W. Andzelm, T. L. Chantawansri, J. L. Lenhart, and F. L. Beyer, Langmuir **27**, 7836 (2011).
[32] J. M. D. Lane, A. E. Ismail, M. Chandross, C. D. Lorenz, and G. S. Grest, Phys. Rev. E **79**, 050501 (2009).
[33] J.-Q. Lin, H.-W. Zhang, Z. Chen, Y.-G. Zheng, Z.-Q. Zhang, and H.-F. Ye, J. Phys. Chem. C **115**, 18991 (2011).
[34] N. N. Poddar and J. G. Amar, J. Chem. Phys. **140**, 244702 (2014).
[35] W. D. Luedtke and U. Landman, J. Phys. Chem. **100**, 13323 (1996).
[36] V. A. Ngo, R. K. Kalia, A. Nakano, and P. Vashishta, J. Phys. Chem. C **116**, 19579 (2012).
[37] S. M. Foiles, M. I. Baskes, and M. S. Daw, Phys. Rev. B **33**, 7983 (1986).
[38] L. Strong and G. M. Whitesides, Langmuir **4**, 546 (1988).
[39] M. J. Hostetler, J. E. Wingate, C.-J. Zhong, J. E. Harris, R. W. Vachet, M. R. Clark, J. D. Londono, S. J. Green,

J. J. Stokes, G. D. Wignall, G. L. Glish, M. D. Porter, N. D. Evans, and R. W. Murray, Langmuir **14**, 17 (1998).

[40] G. H. Woehrle, L. O. Brown, and J. E. Hutchison, J. Am. Chem. Soc. **127**, 2172 (2005).

[41] W. L. Jorgensen, D. S. Maxwell, and J. Tirado-Rives, J. Am. Chem. Soc. **118**, 11225 (1996).

[42] J. G. S. Canchaya, Y. Wang, M. Alcami, F. Martin, and H. F. Busnengo, Phys. Chem. Chem. Phys. **12**, 7555 (2010).

[43] R. Hockney and J. Eastwood, *Computer Simulation Using Particles* (Taylor & Francis, 1988).

[44] M. Tuckerman, B. J. Berne, and G. J. Martyna, J. Chem. Phys. **97**, 1990 (1992).

[45] H. W. Horn, W. C. Swope, J. W. Pitera, J. D. Madura, T. J. Dick, G. L. Hura, and T. Head-Gordon, J. Chem. Phys. **120**, 9665 (2004).

[46] J. L. F. Abascal and C. Vega, J. Chem. Phys. **123**, 234505 (2005).

[47] J.-P. Ryckaert, G. Ciccotti, and H. J. Berendsen, J. Comput. Phys. **23**, 327 (1977).

[48] S. Plimpton, J. Comput. Phys. **117**, 1 (1995).

[49] K. M. Salerno and G. S. Grest, Faraday Discuss. , (2015).

[50] Y. Wang, P. Kanjanaboos, S. McBride, E. Barry, X.-M. Lin, and H. Jaeger, Faraday Discuss. , (2015).

[51] P. Allen and D. Tildesley, *Computer Simulation of Liquids*, Oxford Science Publications (Clarendon Press, 1989).

[52] With a large range of values it may be appropriate to average the Log of the modulus. Applying this procedure to the data reported in [2] Fig. 2 (c) yields a lower estimate of the Young's modulus $E \approx 2 \pm 3$ GPa.